Analysis of Geologically Relevant Metal Porphyrins Using Trapped Ion Mobility Spectrometry−Mass Spectrometry and Theoretical Calculations

Paolo Benigni,[†] Carlos Bravo,[†] J. Martin E. Quirke,[†] John D. DeBord,[†] Alexander M. Mebel,[†] and Francisco Fernandez-Lima*,[†,‡]

[†]Department of Chemistry and Biochemistry and [‡]Biomolecular Sciences Institute, Florida International University, Miami, Florida 33199, United States

S *Supporting Information*

ABSTRACT: The structural characterization of metal porphyrins has been traditionally challenging as a result of their large structural and compositional diversity. In the present paper, we show the advantages of gas-phase, postionization separations for the fast identification and structural characterization of metal octaethylporphyrins (Me−OEP) from complex mixtures using trapped ion mobility spectrometry (TIMS) coupled to ultrahigh-resolution mass spectrometry (FT-ICR MS). TIMS−FT-ICR MS allows for the separation of Me−OEP (Me = Mn, Ni, Zn, V═O, and Ti═O) within a crude oil sample based on accurate mass and mobility signatures (with a mobility resolving power of $R_{IMS} \sim 150-250$). Accurate collision cross sections are reported for Me−OEP in nitrogen as bath gas (CCS_{N_2}). Inspection of the Me−OEP mobility spectra showed a single mobility component distribution for Me−OEP (Me = Mn, Ni, and Zn) and a multi-component distribution for the two metal carbonyls, vanadyl (V═O) and titanyl (Ti═O) Me−OEP. Candidate structures were proposed at the DFT/B3LYP/6-31g(d) level for all Me−OEP mobility bands observed. Inspection of the optimized Me−OEP candidate structures shows that manganese, zinc, and free OEP adopt a planar conformation, the nickel-complexed OEP structure adopts a "ruffled" conformation; and the metal oxide OEP adopts a dome conformation, with carbonyl pointing upward, perpendicular to the plane of the structure.

■ INTRODUCTION

In the early 1930s, Alfred Treibs isolated porphyrins from a range of geological materials, including crude oils, oil shales, coals, and phosphorites.[1−4] The discovery provided strong evidence for the biological origin of crude oil, as well as indicating that crude oil was generated at temperatures below 300 °C. The work by Treibs culminated in the postulation of the Treibs hypothesis that biological molecules underwent a series of transformations in which functional groups were either lost or converted to the appropriate alkyl moieties, as shown in Scheme 1. This hypothesis laid the foundation of organic geochemistry at the molecular level.[5] Subsequently, geoporphyrins have proven to be valuable in oil exploration, where the ratio of nickel/vanadium porphyrins and the ratio of deoxophylloerythroetioporphyrin (DPEP)/etioporphyrin are used as maturation parameters.[6] In addition, the distribution of porphyrins in oils and shales can be used for correlation of crude oils with other crude oils and crude oils with potential source rocks.[7,8]

Geoporhyrins occur with a wide variety of skeletal types, of which DPEP and etioporphyrin (Scheme 1) are the most important. They are typically found as either the vanadyl (V═O) or nickel complexes. Metal-free geoporphyrins do exist in nature but are rare.[9] Likewise, there have been reports of gallium, iron, and manganese porphyrins in coal[10] and copper porphyrins in shale.[11] The vanadyl and nickel porphyrins are the most prevalent metal complexes found in oil and shale;[12] however, these have an unfortunate property of damaging cracking catalysts used in the refining process and are often called the "red peril" of the oil refinery.

Identification of geoporphyrins is traditionally challenging because of the wide variety of structures as well as the complexity of the matrix in which they are typically found. Traditionally, liquid chromatography has been used with X-ray crystallography, ultraviolet−visible (UV−vis),[13] Fourier transform infrared spectroscopy (FTIR), nuclear magnetic resonance (NMR),[14] and inductively coupled plasma mass spectrometry (ICP−MS)[15] for the characterization and quantification of porphyrins.[16] In recent years, mass spectrometry (MS)-based technologies have been developed and used for the molecular characterization of crude oils. Particularly, Fourier transform ion cyclotron resonance mass spectrometry (FT-ICR MS) has been coupled with electrospray ionization (ESI),[17,18] atmospheric pressure photoionization (APPI),[19−22] direct analysis in real time (DART),[23,24] and laser desorption ionization (LDI)[25,26] for the analysis of vanadyl and nickel porphyrins, without the use of pre-separation, as well as structural elucidation by tandem MS techniques using electron-induced dissociation of Fe[(III)] octaethylporphyrin[27] and 405 nm photofragmentation of hemin[+].[28] Although MS techniques are capable of identifying porphyrins by their chemical formula and some structural features by tandem MS, elucidation of the

Scheme 1. Diagram Illustrating the Chemical Changes Outlined in the Treibs Hypothesis[a]
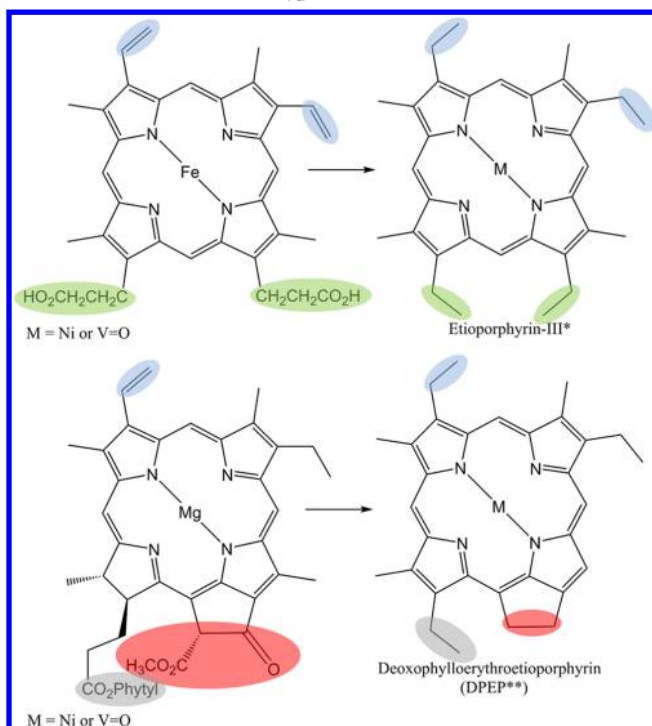
[a]Note the changes in the different functional groups observed.

tridimensional structure and conformation has not been reported.

Molecular characterization of complex mixtures using ion mobility spectrometry coupled to MS (IMS−MS) is rapidly becoming the analytical gold standard that combines the power of ultrahigh-resolution MS with the isomeric separation and structural identification capabilities of IMS.[29−35] Moreover, the IMS measurement, when complemented with theoretical calculations, has proven to be a powerful technique for structural molecular analysis by correlating the ion-neutral, collision cross sections (CCSs) with candidate structures.[36−43] Specifically, we have shown the potential of trapped ion mobility spectrometry (TIMS) for the analysis of small (e.g., polyaromatic hydrocarbons,[44] explosives,[45] and metabolites[46]) and large (e.g., peptides, protein, DNA, and their complexes[47−50]) molecules with IMS resolving powers of up to 400.[46] The advantages of coupling TIMS to FT-ICR MS has been shown for the case of endocrine disruptors,[51] glycans,[52] structural and conformational peptide isomers,[53] and crude oils.[53]

In this study, we use, for the first time, the advantages of TIMS and FT-ICR MS for the separation and structural characterization of metal octaethylporphyrins (Me−OEP) in crude oils. This study provides the first tridimensional characterization of Me−OEP combining accurate collision cross section measurements in nitrogen with candidate structure generation at the DFT/B3LYP level for the characterization of Me−OEP conformational space.

■ EXPERIMENTAL SECTION

Sample Preparation. Octaethylporphyrin (OEP) samples were obtained from Sigma-Aldrich and used as received. Titanyl-OEP was prepared by heating OEP with $TiO(acac)_2$ and phenol following the method by Buchler et al.[54] Samples were dissolved in methylene

chloride and subsequently diluted with methanol with 1% (v/v) acetic acid. A standard reference material of polycyclic aromatic hydrocarbons (PAHs) in coal tar (SRM 1597a) was purchased from the National Institute of Standards and Technology (Gaithersburg, MD) and was diluted 1:100 in 50:50 (v/v) methanol/toluene. A tuning mix mass spectrometry standard (Tunemix, G2421A, Agilent Technologies, Santa Clara, CA) was used as a mobility calibration standard. Details on the Tunemix structures (e.g., m/z 322, K_o = 1.376 cm^2 V^{-1} s^{-1}; m/z 622, K_o = 1.013 cm^2 V^{-1} s^{-1}; and m/z 922, K_o = 0.835 cm^2 V^{-1} s^{-1}) can be found in ref 55. An APPI source (Apollo II, Bruker Daltonics, Inc., Billerica, MA) using a Kr lamp with main emission bands at 10.0 and 10.6 eV was used for all of the analyses. Acetone was used as an APPI dopant (10% by volume).

Structural Separation by TIMS−MS. Details regarding TIMS operation and differences from traditional IMS can be found elsewhere.[53,56,57] Ion mobility separation in the TIMS occurs when ions in the TIMS tunnel experience a drag force as a result of a moving gas of velocity v_g and are compensated by an electric field, which holds the ions stationary within the tunnel. The mobility, K, of an ion in a TIMS cell is described by

$$K = \frac{v_g}{E} = \frac{A}{(V_{elution} - V_{out})} \quad (1)$$

where v_g, E, $V_{elution}$, and V_{out} are the velocity of the gas, applied electric field, elution voltage, and tunnel out voltage, respectively. The constant A is determined from calibration with known standards (e.g., Tunemix and G2421A).

Typical experimental parameters used nitrogen as a bath gas at ca. 300 K, and typical P_1 and P_2 values are 2.6 and 1.0 mbar, respectively. The same radio frequency (RF, 880 kHz and 200−350 V$_{pp}$) was applied to all electrodes, including the entrance funnel, the mobility separating section, and the exit funnel. Mobility values (K) were correlated with CCS (Ω) using the equation

$$\Omega = \frac{(18\pi)^{1/2}}{16} \frac{z}{(k_B T)^{1/2}} \left[\frac{1}{m_I} + \frac{1}{m_b} \right]^{1/2} \frac{1}{K} \frac{760}{P} \frac{T}{273.15} \frac{1}{N^*} \quad (2)$$

where z is the charge of the ion, k_B is the Boltzmann constant, N^* is the number density, and m_I and m_b refer to the masses of the ion and bath gas, respectively.[58]

TIMS−FT-ICR MS Analysis. An orthogonal, commercial APPI source based on the Apollo II design (Bruker Daltonics, Inc., Billerica, MA) with a Kr lamp with main emission bands at 10.0 and 10.6 eV was used. Briefly, sample solutions were introduced into the nebulizer at a rate of 300 μL/min using an external syringe pump. Typical source operating conditions were a 2 L/min dry gas flow rate, a 0.5 bar nebulizer gas pressure, a 220 °C dry gas temperature, and a 300 °C vaporizer temperature. Ions from the APPI source were introduced via a 0.6 mm inner diameter, single-bore glass capillary tube, which is resistively coated across its length, allowing the nebulizer to be maintained at ground potential, while the exit end of the capillary can be independently biased (typical values are −900 and 60−180 V for the entrance and exit, respectively).

TIMS separation used nitrogen as a bath gas at ca. 300 K with the gas flow velocity controlled by the pressure difference between the entrance funnel P_1 = 2.6−3.0 mbar and the exit funnel P_2 = 1.5−1.6 mbar. TIMS voltage sequences were controlled using in-house software, written in National Instruments LabVIEW (version 12.0f3), and synchronized with the FT-ICR MS acquisition program. The TIMS cell was operated using a fill/trap/elute/quench sequence of 300/50/40/10 ms, collecting a single FT-ICR MS spectrum for each mobility trapping step. FT-ICR MS operation was optimized for ion transmission in the m/z 150−1500 range and processed using sin-squared windowing in magnitude mode. TIMS analysis was performed in oversampling mode[53] with a ΔV_{ramp} of 1 V in the range from −25 to −180 V and a V_{step} of 0.2 V; a total of 30 mobility steps were accumulated in the collision cell prior to injection in the ICR cell. FT-ICR MS and TIMS−FT-ICR MS spectra were acquired at 8 000 000 word (6 s transient and R_{MS} = 600 000 at m/z 400, using an average of

Table 1. Experimental Mass (m/z), Mobility (K_o), and CCSs for Me−OEP Studied Using TIMS−FT-ICR MS[a]

Me−OEP	experimental mass (m/z)	theoretical mass (m/z)	formula	mobility, K_0 (cm² s⁻¹ V⁻¹)	CCS (Å²)	theoretical CCS
$[M + H]^+$	535.379	535.379	$[C_{36}H_{47}N_4]^+$	0.850	242	248
$[M + Mn − 2H]^+$	587.294	587.294	$[C_{36}H_{44}N_4Mn]^+$	0.844	244	248
$[M + Ni − H]^+$	591.299	591.299	$[C_{36}H_{45}N_4Ni]^+$	0.846	244	248
$[M + Zn − H]^+$	597.293	597.293	$[C_{36}H_{45}N_4Zn]^+$	0.839	245	247
$[M + VO − H]^+$	600.302	600.303	$[C_{36}H_{45}N_4VO]^+$	0.841	244	249
				0.833	246	248
$[M + TiO − H]^+$	597.307	597.307	$[C_{36}H_{45}N_4TiO]^+$	0.823	249	250
				0.832	247	249

[a]Theoretical CCSs are provided for each Me−OEP candidate structure.

100 scans) and 512 000 word (R_{MS} = 35 000 at m/z 400, using single scan), respectively. Details for data processing can be found elsewhere.[53]

Theoretical Calculations. A pool of Me−OEP candidate structures was obtained from previously reported crystal structures.[59−66] Candidate structures were proposed on the basis of the stoichiometry of the Me−OEP ions observed during the TIMS−FT-ICR MS experiments. Me−OEP structures were protonated at the bridge, nitrogen, and oxygen, for the metal oxide structures, prior to geometry energy optimization and frequency calculation at the B3LYP/6-31g(d) level.[67] Zero-point vibrational energy corrections obtained from the calculations of vibrational frequencies were included in all energies of Me−OEP. Partial atomic charges were calculated using the Merz−Singh−Kollman scheme constrained to the molecular dipole moment.[68,69] Theoretical mobility values were calculated using the 70% diffuse hard sphere scattering (DHSS) model (3 000 000 nitrogen molecules per rotation, three rotations, 92% Maxwell distributed remission velocity, and 70% accommodation) in IMoS software (version 1.06W64d).[70−72] Details on the optimized Me−OEP geometries can be found in the Supporting Information.

RESULTS AND DISCUSSION

Porphyrins typically adopt planar conformations retaining the aromatic properties of the molecule. However, metal chelation in the center of the ring, between the tetrapyrrole subunits, can result in significant conformational shifts, as observed previously by X-ray crystallography.[59−66] In the gas phase, OEP can be ionized using APPI while forming protonated molecules, $[M + H]^+$, as well as radical ions $[M]^{+•}$ as in the case of Mn−OEP. When OEP is chelated with a metal, there is a significant mass shift as well as changes in the isotopic ratio of the molecule, generating a unique mass signal that can be detected using FT-ICR MS (see Table 1). In combination with TIMS, the structural changes as a function of the chelating agent, such as the increase in mass and volume, can also be studied by measuring their CCS (see Figure 1). For example, in comparison of the free OEP and the Mn-, Zn-, and Ni-complexed OEP, an increase in the CCS is observed mainly attributed to the increase in mass and volume. Moreover, in comparison of the V═O- and Ti═O-complexed OEPs, the differences in CCSs are mainly attributed to structural changes because the mass difference is relatively small.

An advantage of the TIMS−FT-ICR MS analysis is the possibility to generate chemical formulas using the high mass accuracy of FT-ICR MS and to measure accurate mobility (or CCS) values using TIMS in a single analysis of a complex mixture. Previous results have shown that the combination of FT-ICR MS with TIMS allows for the identification of a greater number of molecular features, with either targeted[51] or unsupervised[53] analysis of complex mixtures based on their isomeric content. That is, the high isomeric content of complex mixtures (e.g., crude oils) requires the use of complementary,

gas-phase separation tools based on size and mass. The advantage of TIMS−FT-ICR MS analysis for the case of ME−OEP in a complex mixture is shown in Figure 2. The primary heteroatom classes of the coal tar mixture (HC, N, O, and S classes) can be distinguished by the space occupied in the two-dimensional (2D) IMS−MS plot by the different classes shown as the dependence of $1/K_0$ (which scales almost linearly with size for a given family) with m/z. The position in the 2D IMS−MS plot of each class corresponds to a particular structural characteristic; for example, the nitrogen species occupy primarily a region with higher aliphatic content, double bond equivalent (DBE) of 3.5−7.5, while the other three molecular classes, HC, O, and S, fall within a more aromatic region. While free OEP falls within the trend lines for polyaromatic hydrocarbons, the metal chelator in OEP produces a significant mass shift in comparison to the mobility shift. That is, the metal-complexed OEPs fall out of trend in the 2D IMS−MS plot, which facilitates their identification within the complex mixture of polyaromatic hydrocarbons.
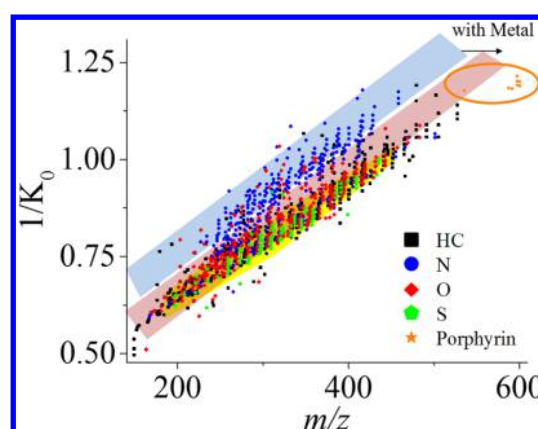
The changes in the Me−OEP structure and size as a function of the metal chelator can be further explored by comparison to candidate structures (Figure 3). Of the different structures examined for OEP, only the radical ion form $[M]^{+•}$ OEP adopts a true planar conformation in the gas phase; however, the protonated form $[M + H]^+$ was favored in the APPI−TIMS−FT-ICR MS experiments. Two potential protonation sites were considered for the free OEP: (i) the carbon that bridges the two pyrrole groups and (ii) a free nitrogen on a pyrrole group. Optimization of the gas-phase structures for both compounds show deviations from planarity, which are evaluated on the basis of the symmetry of the distances between the pyrrole subunits, bridge carbons, dihedral angle between the nitrogen atoms, and angle of the bridge carbon (see Table 2). For the bridge-bound protonation site, changing the hybridization to sp³ causes the carbon to slightly "pucker", increasing the distance from the opposite carbon from 6.9 to 7.0 Å. Binding of free nitrogen induces a much greater structural shift because of steric hindrance, which is due to the addition of a proton within the pocket of OEP. This is observed by the change in the dihedral angle between the nitrogen atoms, which are coplanar in the radical OEP $[M]^{+•}$ and 0° and 1° in the protonated OEP $[M + H]^+$ at the bridge and nitrogen, respectively. The distance between the opposite nitrogen atoms increases from 4.0 to 4.1 Å after protonation. Despite the differences in conformation, both protonated OEP $[M + H]^+$ forms yield a CCS of 248 Å², which is 1−3 Å² greater than the CCS of the radical ion OEP $[M]^{+•}$ form. Note that theoretical deviations from the experimental measurement with the IMoS 70% DHHS model are typically ∼2%. While we cannot discriminate the protonation site based on the CCS values, the
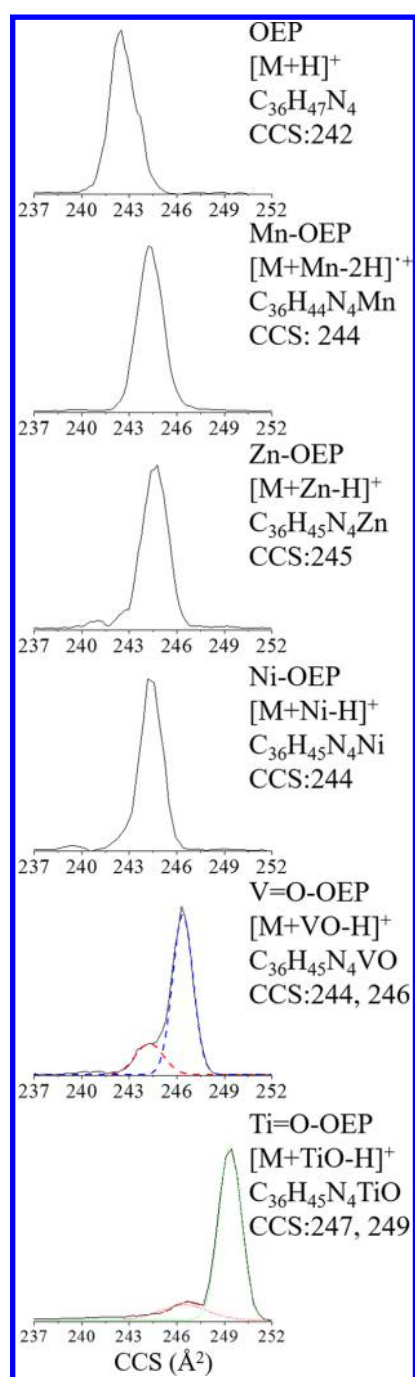
Figure 1. Mobility spectra of Me−OEP obtained using APPI−TIMS−FT-ICR MS. Note the single- and dual-band mobility profiles observed for Mn, Zn, and Ni compared to the vanadyl (V═O) and titanyl (Ti═O), respectively.

Figure 2. Distribution of four commonly encountered molecular classes (HC, N, O, and S) observed in the coal tar APPI−TIMS−FT-ICR MS analysis and the OEP unique space based on their m/z and inverse mobility $1/K_0$. Note the area occupied by OEPs is shifted to a greater m/z than other molecules within the aromatic region of the 2D IMS−MS plot.

protonation of nitrogen is energetically more favorable than the bridge in the metal free OEP by 68 kJ/mol.

Metal binding within the aromatic ring can be challenging to characterize as a result of the insertion of a bulky metal with access to 3d orbitals. Chemically, the binding of the metal is accompanied by the loss of the two hydrogens found within the ring and metal complexation within this pocket formed by the tetrapyrrole unit. Of all of the different OEPs studied, the manganese OEP was the only porphyrin for which the radical species was observed. Optimized candidate structures show that the Mn−OEP porphyrin has a planar conformation, with

symmetric distances between the pyrrole nitrogen atoms ($d =$ 6.8 Å) and a dihedral angle of 0°. The conformations of Zn−OEP and Ni−OEP depend primarily upon the metal rather than the protonation site. For example, Zn−OEP has a mostly planar conformation independent of whether nitrogen or bridge carbon is protonated. Pyrrole protonation is energetically very similar to protonation of the bridge, with the bridge form being 0.18 kJ/mol energetically less favorable than pyrrole. However, protonation of pyrrole induces asymmetry within the molecule, increasing the distances between protonated nitrogen and the opposite nitrogen atom to 4.3 and 3.9 Å compared to the bridge protonated structure that has a distance of 4.1 Å between the opposite nitrogen atoms. In comparison to Mn−OEP and Zn−OEP, the nickel metal is complexed much more tightly, as evidenced by the distances between the nitrogens of 3.8 Å with a protonated bridge and 3.9 Å for the protonated nitrogen in Ni−OEP. Because the distances between the opposite nitrogen atoms are smaller in Ni−OEP, the structure adopts a "ruffled" conformation with two bridge carbons pointing upward and two pointing downward. For the bridge protonated structure, the angle between the bridge and pyrroles is reduced to 143° for the protonated carbon and 163° for the other bridges. Of the two candidate Ni−OEP structures, the bridge structure has a lower energy than N protonated by 28 kJ/mol.

When free OEP binds to a metal oxide ligand, as in the case of titanyl (Ti═O) and vanadyl (V═O), the high resolving power of TIMS ($R_{IMS} \approx 200$) showed two distinct bands in the mobility spectra. One hypothesis explored was that the two mobility bands could be attributed to two distinct dome conformations, one with the carbonyl pointing out of the dome and a second pointing inward. However, theoretical calculations showed that only the carbonyl pointing out of the dome was energetically favorable and that a local energy minima could not be found when carbonyl was pointing inward, making the theoretical characterization of this state challenging. A second hypothesis explored was that the ionization event simultaneously generates molecular ions with different protonation sites. Three sites were considered, protonating the bridge, nitrogen, and carbonyl (Figure 4). Similar to previous results, the protonation of pyrrole nitrogen is the least favorable, while the protonation of oxide was significantly more favorable, by
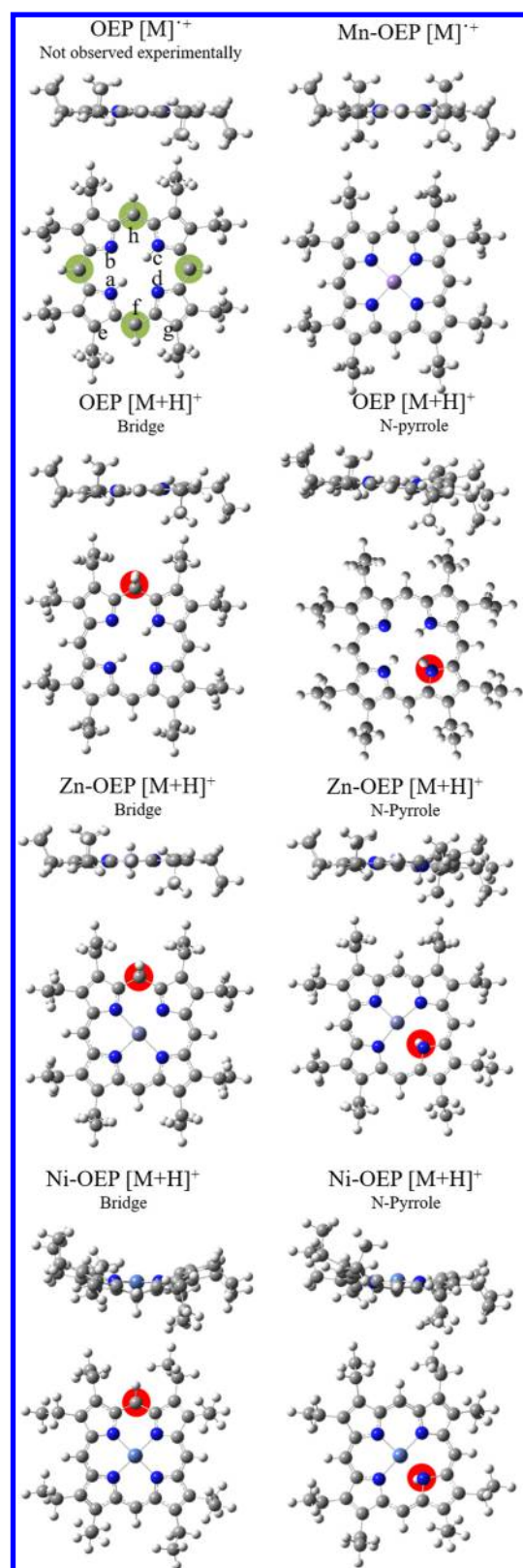
Figure 3. Projections of the three-dimensional (3D)-optimized structures for the different OEPs. The radical OEP, not observed experimentally, is labeled with the bridge carbons (green circles) as well as the notation for the distances and angles shown in Table 2. Protonation sites are highlighted in red circles. Note that the deviations from planarity depend upon the protonation site. More details can be found in Table 2.

Table 2. Results from the Theoretical Calculations, Illustrating the Changes in Bond Length between the Nitrogen Atoms in Pyrrole (See Figure 3 for Labels), the Bridge Carbons, the Dihedral Angle between Nitrogen, and the Angle between the Bridge[a]

	$\overleftrightarrow{ad}$ (Å)	$\overleftrightarrow{fh}$ (Å)	∠abcd (deg)	∠efg (deg)
OEP	4.04	6.86	0.0	176
OEP bridge	4.09	7.00	0.1	175
	4.2			
OEP pyrrole	4.11	6.88	1.2	176
Mn−OEP	3.92	6.83	0.1	178
Zn−OEP bridge	3.83	6.93	0.7	175−9
		6.83		
Zn−OEP pyrrole	3.93	6.87	0.0	172−3
	4.30			
Ni−OEP bridge	3.83	6.50	0.1	143
		6.51		163
Ni−OEP pyrrole	3.94	6.73	0.2	163−6
	3.86			
VO−OEP pyrrole	4.01	6.87	4.5	172−6
	4.18			
VO−OEP bridge	4.07	6.91	0.6	163
		6.81		173−6
VO−OEP oxygen	3.97	6.83	2.7	177
TiO−OEP pyrrole	4.06	6.89	4.5	170
	4.24			176
TiO−OEP bridge	4.12	6.83	0.5	166
		6.93		174−6
TiO−OEP oxygen	4.01	6.85	0.0	176

[a]Note how each metal and protonation side greatly affects the conformation of the porphyrin.

approximately 30−65 kJ/mol. For the vanadyl OEP, the energy differences between the bridge protonation and the oxide are not significantly different and both compounds may be observed experimentally, with a greater relative abundance probably for the lower energy isomer. However, the optimized titanyl OEP structures show a more significant energy barrier between protonated oxide and bridge. Results showed that, although there are significant differences in energy between these structures, the differences in the theoretical CCS do not account for the experimental observations. That is, in both cases, the experimental difference in CCS is between 2 and 3 Å^2, and the high resolving power of TIMS allows these different states to be resolved. Further improvements on the theoretical CCS calculators are needed when the IMS resolving power exceeds 200 for the analysis of Me−OEP.

These results highlight the potential of fast gas-phase, postionization separation and characterization of porphyrins and their different conformations, in either purified or crude samples using TIMS−FT-ICR MS and theoretical calculations. That is, the high-resolution ion mobility separation, combined with chemical formula generation based on accurate mass and the theoretical tools, enables the identification and structural characterization of porphyrins as a function of the metal chelate or other modifications to the ring that may cause conformational shifts. Notice that this methodology can be further adapted for the quantification of Me−OEP within complex mixtures in a single analysis without the need for pre-fractionation.
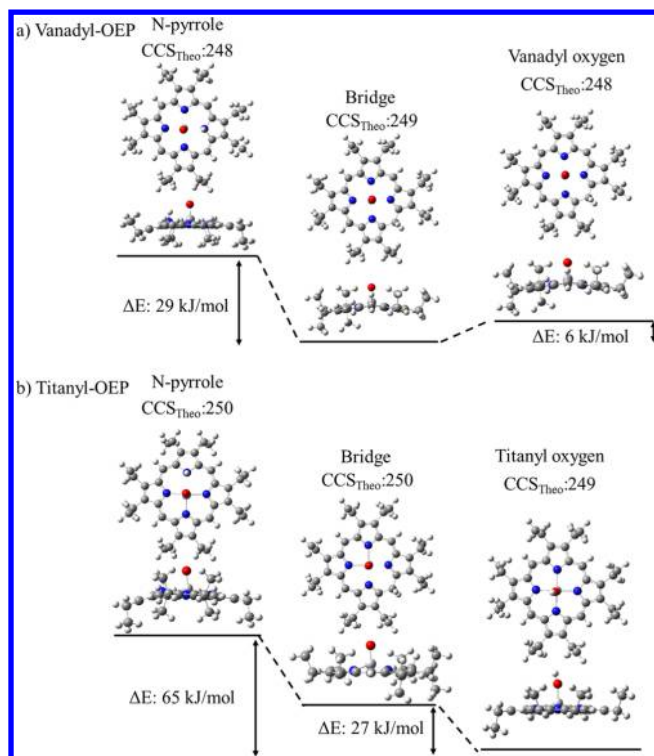
Figure 4. Energy landscape diagram showing the change in energy for each protonation site calculated for the vanadyl and titanyl structures. Note that the theoretical CCSs are fairly similar for all of the structures, even though each structure is unique and the energies are different.

CONCLUSION

This work illustrates the use of TIMS−FT-ICR MS for the gas-phase separation and characterization of free OEP and OEP complexed with manganese, nickel, zinc, vanadyl, and titanyl. Upon metal binding, changes in CCS are observed as a function of the metal complexed within the pocket of the OEP ring, with single, high resolving power ($R_{IMS} \sim 150−250$) bands observed for OEP (H$_2$, Mn, Ni, and Zn), while two IMS bands are observed for the metal oxides vanadyl and titanyl OEP. Experimental results from APPI−TIMS−FT-ICR MS show that the metal-complexed OEPs have unique shifts in m/z and CCS, which allows for their identification within a complex mixture of aromatic molecules from coal tar. The shifts in collisional cross section for Me−OEP as a function of Me suggest that there are significant conformational changes upon metal binding. Candidate structures were proposed for the different Me−OEP as a function of the Me and protonation site. A good agreement is observed between the most energetically favorable candidate structures and the measured CCS. Results also show the need for the development of new and better CCS calculators (<2% error) when using high-resolution IMS instrumentation, such as TIMS. This work provides the proof of principle for fast identification and characterization of the conformational space of Me−OEP within complex mixtures.

ASSOCIATED CONTENT

ⓢ Supporting Information

The Supporting Information is available free of charge on the ACS Publications website at DOI: 10.1021/acs.energy-fuels.6b02388.

Details on the optimized Me−OEP geometries (PDF)

AUTHOR INFORMATION

Corresponding Author

*Telephone: 305-348-2037. Fax: 305-348-3772. E-mail: fernandf@fiu.edu.

Notes

The authors declare no competing financial interest.

ACKNOWLEDGMENTS

REFERENCES

(1) Treibs, A. *Liebigs Ann. Chem.* **1935**, *520* (1), 144−150.

(2) Treibs, A. *Liebigs Ann. Chem.* **1934**, *509* (1), 103−114.

(3) Treibs, A. *Justus Liebigs Ann. Chem.* **1934**, *510* (1), 42−62.

(4) Treibs, A.; Dinelli, D. *Liebigs Ann. Chem.* **1935**, *517* (1), 170−172.

(5) Treibs, A. *Angew. Chem.* **1936**, *49* (38), 682−686.

(6) Eglinton, G.; Maxwell, J. R.; Evershed, R. P.; Barwise, A. J. G. *Interdiscip. Sci. Rev.* **1985**, *10* (3), 222−236.

(7) Ocampo, R.; Riva, A.; Trendel, J. M.; Riolo, J.; Callot, H. J.; Albrecht, P. *Energy Fuels* **1993**, *7* (2), 191−193.

(8) Philp, R. P. Oil−Oil and Oil−Source Rock Correlations: Techniques. In *Organic Geochemistry*; Engel, M. H., Macko, S. A., Eds.; Springer: Boston, MA, 1993; Vol. *11*, Chapter 19, pp 445−460, DOI: 10.1007/978-1-4615-2890-6_19.

(9) Quirke, J. M. E.; Dale, T.; Britton, E. D.; Yost, R. A.; Trichet, J.; Belayouni, H. *Org. Geochem.* **1990**, *15* (2), 169−177.

(10) Bonnett, R.; Burke, P. J.; Czechowski, F. Metalloporphyrins in Lignite, Coal, and Calcite. In *Metal Complexes in Fossil Fuels*; Filby, R. H., Branthaver, J. F., Eds.; American Chemical Society (ACS): Washington, D.C., 1987; ACS Symposium Series, Vol. *344*, Chapter 11, pp 173−185, DOI: 10.1021/bk-1987-0344.ch011.

(11) Kashiyama, Y.; Ogawa, N. O.; Nomoto, S.; Kitazato, H.; Ohkouchi, N. *Earth, Life, Isot.* **2010**, 313−335.

(12) Quirke, J. M. E. Rationalization for the Predominance of Nickel and Vanadium Porphyrins in the Geosphere. In *Metal Complexes in Fossil Fuels*; Filby, R. H., Branthaver, J. F., Eds.; American Chemical Society (ACS): Washington, D.C., 1987; ACS Symposium Series, Vol. *344*, Chapter 4, pp 74−83, DOI: 10.1021/bk-1987-0344.ch004.

(13) Sugihara, J. M.; Bean, R. M. *J. Chem. Eng. Data* **1962**, *7* (2), 269−271.

(14) Buenrostro-Gonzalez, E.; Andersen, S. I.; Garcia-Martinez, J. A.; Lira-Galeana, C. *Energy Fuels* **2002**, *16* (3), 732−741.

(15) Biggs, W. R.; Fetzer, J. C.; Brown, R. J.; Reynolds, J. G. *Liq. Fuels Technol.* **1985**, *3* (4), 397−421.

(16) Zhao, X.; Xu, C.; Shi, Q. Porphyrins in Heavy Petroleums: A Review. In *Structure and Modeling of Complex Petroleum Mixtures*; Xu, C., Shi, Q., Eds.; Springer: Berlin, Germany, 2015; Vol. *168*, pp 39−70, DOI: 10.1007/430_2015_189.

(17) Zhao, X.; Liu, Y.; Xu, C. M.; Yan, Y. Y.; Zhang, Y. H.; Zhang, Q. Y.; Zhao, S. Q.; Chung, K.; Gray, M. R.; Shi, Q. *Energy Fuels* **2013**, *27* (6), 2874−2882.

(18) Kekalainen, T.; Pakarinen, J. M. H.; Wickstrom, K.; Lobodin, V. V.; McKenna, A. M.; Janis, J. *Energy Fuels* **2013**, *27* (4), 2002−2009.

(19) McKenna, A. M.; Purcell, J. M.; Rodgers, R. P.; Marshall, A. G. *Energy Fuels* **2009**, *23* (4), 2122−2128.

(20) Qian, K.; Edwards, K. E.; Mennito, A. S.; Walters, C. C.; Kushnerick, J. D. *Anal. Chem.* **2010**, *82* (1), 413−9.

(21) Swider, P.; Lewtak, J. P.; Gryko, D. T.; Danikiewicz, W. *J. Mass Spectrom.* **2013**, *48* (10), 1116−24.

(22) McKenna, A. M.; Williams, J. T.; Putman, J. C.; Aeppli, C.; Reddy, C. M.; Valentine, D. L.; Lemkau, K. L.; Kellermann, M. Y.; Savory, J. J.; Kaiser, N. K.; Marshall, A. G.; Rodgers, R. P. *Energy Fuels* **2014**, *28* (4), 2454−2464.

(23) Romao, W.; Tose, L. V.; Vaz, B. G.; Sama, S. G.; Lobinski, R.; Giusti, P.; Carrier, H.; Bouyssiere, B. *J. Am. Soc. Mass Spectrom.* **2016**, *27* (1), 182−5.

(24) Ren, L. M.; Han, Y. H.; Zhang, Y. H.; Zhang, Y. F.; Meng, X. H.; Shi, Q. *Energy Fuels* **2016**, *30* (6), 4486−4493.

(25) Cho, Y.; Witt, M.; Jin, J. M.; Kim, Y. H.; Nho, N. S.; Kim, S. *Energy Fuels* **2014**, *28* (11), 6699−6706.

(26) Kim, E.; Cho, E.; Moon, S.; Park, J. I.; Kim, S. *Energy Fuels* **2016**, *30* (4), 2932−2940.

(27) Kaczorowska, M. A.; Cooper, H. J. *Chem. Commun.* **2011**, *47* (1), 418−20.

(28) Charkin, O. P.; Klimenko, N. M.; Nguyen, P. T.; Charkin, D. O.; Mebel, A. M.; Lin, S. H.; Wang, Y. S.; Wei, S. C.; Chang, H. C. *Chem. Phys. Lett.* **2005**, *415* (4−6), 362−369.

(29) Fernandez-Lima, F. A.; Becker, C.; McKenna, A. M.; Rodgers, R. P.; Marshall, A. G.; Russell, D. H. *Anal. Chem.* **2009**, *81* (24), 9941−7.

(30) Fasciotti, M.; Lalli, P. M.; Klitzke, C. F.; Corilo, Y. E.; Pudenzi, M. A.; Pereira, R. C. L.; Bastos, W.; Daroda, R. J.; Eberlin, M. N. *Energy Fuels* **2013**, *27* (12), 7277−7286.

(31) Lalli, P. M.; Corilo, Y. E.; Rowland, S. M.; Marshall, A. G.; Rodgers, R. P. *Energy Fuels* **2015**, *29* (6), 3626−3633.

(32) Ahmed, A.; Cho, Y. J.; No, M. H.; Koh, J.; Tomczyk, N.; Giles, K.; Yoo, J. S.; Kim, S. *Anal. Chem.* **2011**, *83* (1), 77−83.

(33) Ahmed, A.; Cho, Y.; Giles, K.; Riches, E.; Lee, J. W.; Kim, H. I.; Choi, C. H.; Kim, S. *Anal. Chem.* **2014**, *86* (7), 3300−3307.

(34) Ponthus, J.; Riches, E. *Int. J. Ion Mobility Spectrom.* **2013**, *16* (2), 95−103.

(35) Santos, J. M.; Galaverna, R. D.; Pudenzi, M. A.; Schmidt, E. M.; Sanders, N. L.; Kurulugama, R. T.; Mordehai, A.; Stafford, G. C.; Wisniewski, A.; Eberlin, M. N. *Anal. Methods* **2015**, *7* (11), 4450−4463.

(36) Fernandez-Lima, F. A.; Blase, R. C.; Russell, D. H. *Int. J. Mass Spectrom.* **2010**, *298* (1−3), 111−118.

(37) Fernandez-Lima, F. A.; Wei, H.; Gao, Y. Q.; Russell, D. H. *J. Phys. Chem. A* **2009**, *113* (29), 8221−8234.

(38) Valentine, S. J.; Counterman, A. E.; Clemmer, D. E. *J. Am. Soc. Mass Spectrom.* **1999**, *10* (11), 1188−1211.

(39) Tao, L.; McLean, J. R.; McLean, J. A.; Russell, D. H. *J. Am. Soc. Mass Spectrom.* **2007**, *18* (7), 1232−8.

(40) Bush, M. F.; Hall, Z.; Giles, K.; Hoyes, J.; Robinson, C. V.; Ruotolo, B. T. *Anal. Chem.* **2010**, *82* (22), 9557−65.

(41) Jarrold, M. F. *Annu. Rev. Phys. Chem.* **2000**, *51* (1), 179−207.

(42) Murray, M. M.; Krone, M. G.; Bernstein, S. L.; Baumketner, A.; Condron, M. M.; Lazo, N. D.; Teplow, D. B.; Wyttenbach, T.; Shea, J. E.; Bowers, M. T. *J. Phys. Chem. B* **2009**, *113* (17), 6041−6.

(43) Baumketner, A.; Bernstein, S. L.; Wyttenbach, T.; Bitan, G.; Teplow, D. B.; Bowers, M. T.; Shea, J. E. *Protein Sci.* **2006**, *15* (3), 420−428.

(44) Castellanos, A.; Benigni, P.; Hernandez, D. R.; DeBord, J. D.; Ridgeway, M. E.; Park, M. A.; Fernandez-Lima, F. *Anal. Methods* **2014**, *6* (23), 9328−9332.

(45) McKenzie-Coe, A.; DeBord, J. D.; Ridgeway, M.; Park, M.; Eiceman, G.; Fernandez-Lima, F. *Analyst* **2015**, *140* (16), 5692−9.

(46) Adams, K. J.; Montero, D.; Aga, D.; Fernandez-Lima, F. *Int. J. Ion Mobility Spectrom.* **2016**, *19* (2−3), 69−76.

(47) Schenk, E. R.; Almeida, R.; Miksovska, J.; Ridgeway, M. E.; Park, M. A.; Fernandez-Lima, F. *J. Am. Soc. Mass Spectrom.* **2015**, *26* (4), 555−63.

(48) Schenk, E. R.; Mendez, V.; Landrum, J. T.; Ridgeway, M. E.; Park, M. A.; Fernandez-Lima, F. *Anal. Chem.* **2014**, *86* (4), 2019−24.

(49) Schenk, E. R.; Ridgeway, M. E.; Park, M. A.; Leng, F.; Fernandez-Lima, F. *Anal. Chem.* **2014**, *86* (2), 1210−4.

(50) Benigni, P.; Marin, R.; Molano-Arevalo, J. C.; Garabedian, A.; Wolff, J. J.; Ridgeway, M. E.; Park, M. A.; Fernandez-Lima, F. *Int. J. Ion Mobility Spectrom.* **2016**, *19* (2−3), 95−104.

(51) Benigni, P.; Thompson, C. J.; Ridgeway, M. E.; Park, M. A.; Fernandez-Lima, F. *Anal. Chem.* **2015**, *87* (8), 4321−5.

(52) Pu, Y.; Ridgeway, M. E.; Glaskin, R. S.; Park, M. A.; Costello, C. E.; Lin, C. *Anal. Chem.* **2016**, *88* (7), 3440−3.

(53) Benigni, P.; Fernandez-Lima, F. *Anal. Chem.* **2016**, *88* (14), 7404−12.

(54) Buchler, J. W.; Eikelmann, G.; Puppe, L.; Rohbock, K.; Schneehage, H. H.; Weck, D. *Liebigs Ann. Chem.* **1971**, *745* (1), 135−151.

(55) Flanagan, L. A. Mass Spectrometry Calibration Using Homogeneously Substituted Fluorinated Triazatriphosphorines. U.S. Patent 5,872,357 A, Feb 16, 1999; pp 19.

(56) Fernandez-Lima, F. A.; Kaplan, D. A.; Park, M. A. *Rev. Sci. Instrum.* **2011**, *82* (12), 126106.

(57) Fernandez-Lima, F.; Kaplan, D. A.; Suetering, J.; Park, M. A. *Int. J. Ion Mobility Spectrom.* **2011**, *14* (2−3), 93−98.

(58) McDaniel, E. W.; Mason, E. A. *Mobility and Diffusion of Ions in Gases*; John Wiley and Sons, Inc.: New York, 1973; pp 381.

(59) Cheng, B.; Scheidt, W. R. *Acta Crystallogr., Sect. C: Cryst. Struct. Commun.* **1995**, *51* (5), 825−828.

(60) Molinaro, F. S.; Ibers, J. A. *Inorg. Chem.* **1976**, *15* (9), 2278−2283.

(61) Meyer, E. F., Jr. *Acta Crystallogr., Sect. B: Struct. Crystallogr. Cryst. Chem.* **1972**, *28* (7), 2162−2167.

(62) Cullen, D. L.; Meyer, E. F. *J. Am. Chem. Soc.* **1974**, *96* (7), 2095−2102.

(63) Brennan, T. D.; Scheidt, W. R.; Shelnutt, J. A. *J. Am. Chem. Soc.* **1988**, *110* (12), 3919−3924.

(64) Guilard, R.; Latour, J. M.; Lecomte, C.; Marchon, J. C.; Protas, J.; Ripoll, D. *Inorg. Chem.* **1978**, *17* (5), 1228−1237.

(65) Lauher, J. W.; Ibers, J. A. *J. Am. Chem. Soc.* **1973**, *95* (16), 5148−52.

(66) Cullen, D. L.; Meyer, E. F., Jr. *Acta Crystallogr., Sect. B: Struct. Crystallogr. Cryst. Chem.* **1976**, *32* (8), 2259−2269.

(67) Montgomery, J. A., Jr; Frisch, M. J.; Ochterski, J. W.; Petersson, G. A. *J. Chem. Phys.* **1999**, *110* (6), 2822−2827.

(68) Singh, U. C.; Kollman, P. A. *J. Comput. Chem.* **1984**, *5* (2), 129−145.

(69) Besler, B. H.; Merz, K. M.; Kollman, P. A. *J. Comput. Chem.* **1990**, *11* (4), 431−439.

(70) Larriba, C.; Hogan, C. J. *J. Comput. Phys.* **2013**, *251*, 344−363.

(71) Larriba, C.; Hogan, C. J., Jr. *J. Phys. Chem. A* **2013**, *117* (19), 3887−901.

(72) Larriba-Andaluz, C.; Fernandez-Garcia, J.; Ewing, M. A.; Hogan, C. J., Jr.; Clemmer, D. E. *Phys. Chem. Chem. Phys.* **2015**, *17* (22), 15019−29.